

# Selective and Efficient Gd-Doped BiVO<sub>4</sub> Photoanode for Two-Electron Water Oxidation to H<sub>2</sub>O<sub>2</sub>

Ji Hyun Baek,<sup>†,‡,⊥</sup> Thomas Mark Gill,<sup>†,⊥</sup> Hadi Abroshan,<sup>§,⊥</sup> Sangwook Park,<sup>†</sup> Xinjian Shi,<sup>†</sup> Jens Nørskov,<sup>§,||</sup> Hyun Suk Jung,<sup>\*,‡,⊥</sup> Samira Siahrostami,<sup>\*,§,⊥</sup> and Xiaolin Zheng<sup>\*,†,⊥</sup>

<sup>†</sup>Department of Mechanical Engineering, Stanford University, Stanford, California 94305, United States

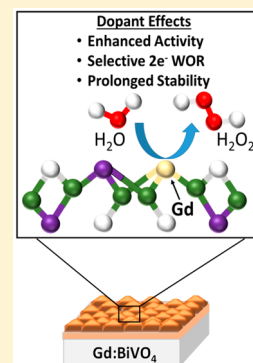
<sup>‡</sup>School of Advanced Materials Science & Engineering, Sungkyunkwan University, Suwon 16419, Republic of Korea

<sup>§</sup>SUNCAT Center for Interface Science and Catalysis, Department of Chemical Engineering, Stanford University, 443 Via Ortega, Stanford, California 94305, United States

<sup>||</sup>SUNCAT Center for Interface Science and Catalysis, SLAC National Accelerator Laboratory, 2575 Sand Hill Road, Menlo Park, California 94305, United States

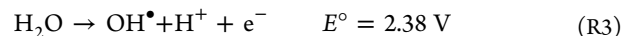
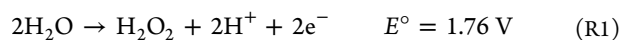
## Supporting Information

**ABSTRACT:** Photoelectrochemical oxidation of water presents a pathway for sustainable production of hydrogen peroxide (H<sub>2</sub>O<sub>2</sub>). Two-electron water oxidation toward H<sub>2</sub>O<sub>2</sub>, however, competes with the popular four-electron process to form oxygen and one-electron water oxidation to form OH radical. To date, bismuth vanadate (BiVO<sub>4</sub>) has been shown to exhibit promising selectivity toward H<sub>2</sub>O<sub>2</sub>, especially under illumination, but it suffers from high overpotential and notoriously poor stability. Herein, using density functional theory calculations, we predict that doping BiVO<sub>4</sub> with optimal concentrations of gadolinium (Gd) not only enhances its activity for H<sub>2</sub>O<sub>2</sub> production but also improves its stability. Experimentally, we demonstrate that intermediate amounts of Gd doping (6–12%) reduce the onset potential of BiVO<sub>4</sub> for H<sub>2</sub>O<sub>2</sub> production by ~110 mV while achieving a Faradaic efficiency of ~99.5% under illumination and prolonging the catalytic lifetime by more than a factor of 20 at 2.0 V vs RHE under illumination.



Hydrogen peroxide (H<sub>2</sub>O<sub>2</sub>) is a strong and green oxidizer and is widely used for applications ranging from electronics fabrication to chemical feedstock synthesis and water purification. Currently, production of H<sub>2</sub>O<sub>2</sub> is centralized via an energy-intensive anthraquinone process.<sup>1</sup> Recently, distributed on-site production of H<sub>2</sub>O<sub>2</sub> has gained interest as a low-cost alternative that also mitigates the need for transport and distribution.<sup>2,3</sup> In particular, photoelectrochemical (PEC) production of H<sub>2</sub>O<sub>2</sub> is highly desirable as it converts solar energy into a valuable liquid chemical.<sup>4</sup> Additionally, evolving H<sub>2</sub>O<sub>2</sub> through water oxidation at the photoanode can be combined with cathodic hydrogen evolution to improve overall PEC cell efficiency and reduce production cost.<sup>4–7</sup>

One of the major challenges for water oxidation to H<sub>2</sub>O<sub>2</sub> is achieving high selectivity. Water oxidation proceeds through three competing pathways: two-electron transfer for H<sub>2</sub>O<sub>2</sub> production (reaction R1), the popular four-electron transfer for oxygen evolution (reaction R2), and one-electron transfer to form hydroxyl radicals (reaction R3)<sup>8</sup>



where the standard redox potentials are taken from ref 9. Selectivity for H<sub>2</sub>O<sub>2</sub> production (reaction R1) over reaction R2 and reaction R3 has been experimentally investigated over many metal oxides, such as MnO<sub>x</sub>,<sup>6,10</sup> BiVO<sub>4</sub>,<sup>11,12</sup> WO<sub>3</sub>,<sup>8,13</sup> and TiO<sub>2</sub>.<sup>14,15</sup> To date, bismuth vanadate (BiVO<sub>4</sub>) has been shown to exhibit the highest selectivity toward H<sub>2</sub>O<sub>2</sub> among all metal oxides,<sup>12,13,16</sup> consistent with the observation that BiVO<sub>4</sub> has sluggish oxygen evolution reaction (reaction R2) kinetics.<sup>17</sup> Despite its low electron mobility (~10<sup>-2</sup> cm<sup>2</sup>/V-s) and small hole collection (~100 nm) depth, BiVO<sub>4</sub> has been extensively studied as a photoanode candidate for oxygen evolution (reaction R2) due to its visible light absorption properties (up to ~520 nm).<sup>18–23</sup> However, for H<sub>2</sub>O<sub>2</sub> production, BiVO<sub>4</sub> has two other major limitations: a higher experimental overpotential (~400 mV) for reaction R1 than

Received: February 4, 2019

Accepted: February 15, 2019

Published: February 15, 2019

other metal oxides and poor stability.<sup>17,24–27</sup> There is a great need to enhance the stability and activity of BiVO<sub>4</sub> while maintaining its selectivity toward H<sub>2</sub>O<sub>2</sub>, a prerequisite for making distributed solar H<sub>2</sub>O<sub>2</sub> production viable.

Herein, we theoretically and experimentally demonstrate that doping BiVO<sub>4</sub> with an optimal amount of the rare earth element gadolinium (Gd) not only reduces the overpotential for H<sub>2</sub>O<sub>2</sub> production but also prolongs BiVO<sub>4</sub> stability under high applied bias. We chose Gd based on its unique electronic structure and material properties: its half-filled 4f valence shell suggests elemental stability, while the metallicity of Gd suggests good electrical conductivity. Furthermore, Gd is substantially more oxyphilic than Bi,<sup>27,28</sup> suggesting that Gd will strongly bind oxygen in BiVO<sub>4</sub>, inhibiting the dissolution of VO<sub>4</sub><sup>3–</sup> anions and thereby addressing a primary source of poor stability for BiVO<sub>4</sub>. Our density functional theory (DFT) calculations reveal that a moderate amount of Gd doping makes several facets of BiVO<sub>4</sub> more active for H<sub>2</sub>O<sub>2</sub> production. Moreover, our calculations demonstrate that the presence of Gd increases the energy barrier for VO<sub>4</sub><sup>3–</sup> dissolution, indicating enhanced stability for BiVO<sub>4</sub> upon Gd doping. Experimentally, we synthesized and characterized BiVO<sub>4</sub> films with various amounts of Gd dopant. Under optimal Gd doping concentrations, the overpotential for H<sub>2</sub>O<sub>2</sub> production is reduced by ~110 mV as compared to undoped BiVO<sub>4</sub> under dark conditions. Furthermore, the selectivity of BiVO<sub>4</sub> is slightly improved from 64% in undoped BiVO<sub>4</sub> to 78% in 6% Gd-doped BiVO<sub>4</sub> at 3.1 V vs RHE in the dark. Finally, the optimized Gd-doped BiVO<sub>4</sub> thick film (~100 nm) shows high performance as a photoanode: under 1 sun illumination, it achieves a current density of 5.2 mA/cm<sup>2</sup> at 2.6 V vs RHE while yielding a peak Faradaic efficiency (FE) of ~99.5% for H<sub>2</sub>O<sub>2</sub> production and a substantially prolonged catalytic lifetime.

**Theoretical Calculation of Activity and Selectivity of Gd-Doped BiVO<sub>4</sub> Catalysts.** The activity and selectivity of a catalyst for two-electron water oxidation toward H<sub>2</sub>O<sub>2</sub> (reaction R1) are influenced by the thermodynamics and kinetics of reaction R1 and its competing reactions R2 and R3. A recent theoretical study by Siahrostami et al. indicates that the adsorption energies of oxygen intermediates, specifically O\* ( $\Delta G_{O^*}$ ) and OH\* ( $\Delta G_{OH^*}$ ), are key parameters in determining catalytic activity and selectivity toward H<sub>2</sub>O<sub>2</sub> (reaction R1) rather than the byproducts, O<sub>2</sub> (reaction R2) and OH radical (reaction R3).<sup>8</sup> On the basis of purely thermodynamic considerations, H<sub>2</sub>O<sub>2</sub> synthesis is favored when  $\Delta G_{OH^*}$  is between 1.6 and 2.4 eV and  $\Delta G_{O^*}$  is larger than 3.5 eV. When  $\Delta G_{OH^*} = 1.76$  eV, optimal conditions toward H<sub>2</sub>O<sub>2</sub> synthesis with zero overpotential are achieved.<sup>29</sup> Alternatively, catalysts with  $\Delta G_{OH^*} < 1.6$  or  $> 2.4$  eV preferentially evolve O<sub>2</sub> or OH radical, respectively.<sup>16,30</sup>

Previous experimental results show that BiVO<sub>4</sub> has an overpotential of around 350–450 mV for producing H<sub>2</sub>O<sub>2</sub><sup>16</sup> because OH\* binds weakly on most facets of BiVO<sub>4</sub>. Even for the most active (111) facet of BiVO<sub>4</sub>,  $\Delta G_{OH^*}$  is 1.95 eV, corresponding to a minimum overpotential of 190 mV. The overpotential of BiVO<sub>4</sub> for H<sub>2</sub>O<sub>2</sub> production in theory can be reduced by incorporating dopants that strengthen the binding of OH\* to the catalyst surface, pushing the performance toward the tip of the activity volcano plot at  $\Delta G_{OH^*} = 1.76$  eV.<sup>16</sup>

Here, we theoretically calculate the effect of the Gd dopant on the  $\Delta G_{OH^*}$  value of various facets of BiVO<sub>4</sub>. Because BiVO<sub>4</sub>

films prepared experimentally are typically polycrystalline, we consider all possible low index facets of BiVO<sub>4</sub> including (001), (101), (011), and (111). Figure 1b,c plots the calculated  $\Delta G_{OH^*}$  and overpotentials for these facets of BiVO<sub>4</sub>. It should be noted that the surface structures of (001), (101), and (011) facets are well-defined and that the

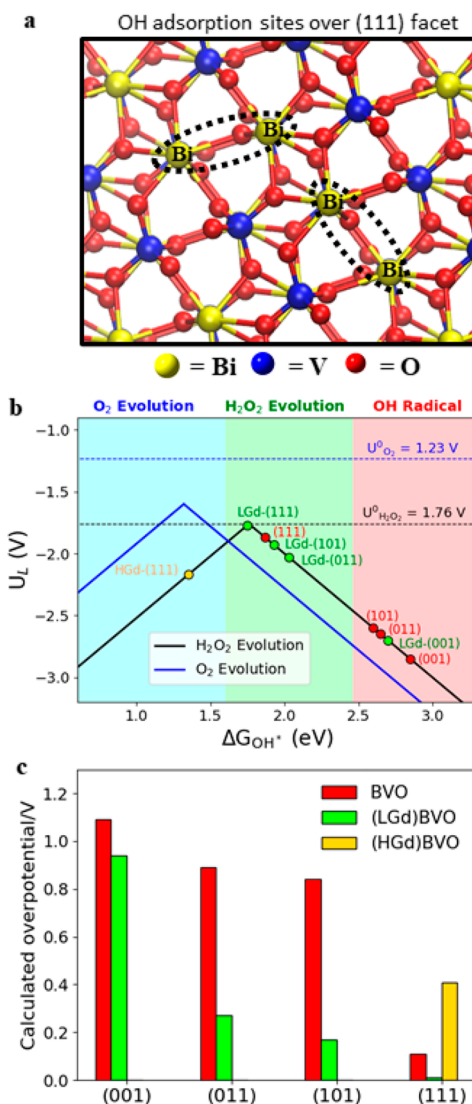


**Figure 1.** Theoretical study of the activity and selectivity of BiVO<sub>4</sub> for two-electron water oxidation toward H<sub>2</sub>O<sub>2</sub>. (a) Top view of the (111) facet of BiVO<sub>4</sub>. The two Bi–Bi bridge sites capable of adsorbing the reaction intermediates are shown (dotted black ovals). Color code: Bi, yellow; V, blue; O, red. (b) Activity volcano plots based on calculated limiting potentials as a function of adsorption energies of OH\* ( $\Delta G_{OH^*}$ ) for 2e<sup>–</sup> and 4e<sup>–</sup> water oxidation to evolve hydrogen peroxide (black) and oxygen (blue). The corresponding equilibrium potentials for the reactions are shown (dashed lines). Replacement of a surface Bi atom increases the facets' activity for H<sub>2</sub>O<sub>2</sub> synthesis (compare red and green points). In particular, the low Gd concentration on (111) facets (denoted LGd-(111)) creates Bi–Gd bridges, which are near the peak of the volcano, indicating high activity for 2e<sup>–</sup> water oxidation. An increase in Gd concentration to produce Gd–Gd bridges shifts the activity of the (111) facet toward the oxygen evolution reaction (HGd-(111), yellow points). (c) Calculated overpotential for the synthesis of H<sub>2</sub>O<sub>2</sub> over different facets.

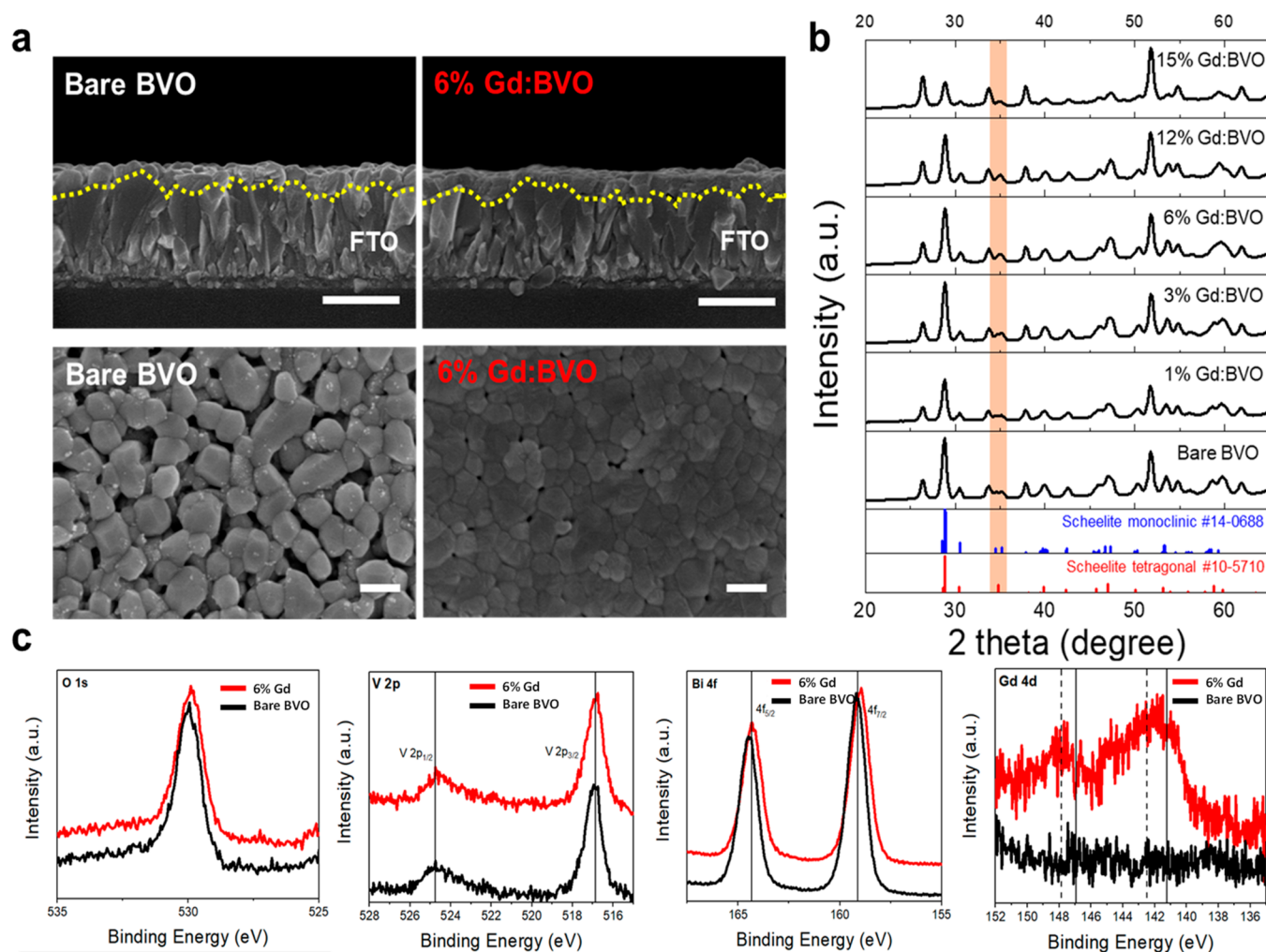


**Figure 2.** Characterizations of undoped and Gd-doped  $\text{BiVO}_4$ . (a) Side- and top-view SEM images of bare BVO and 6% Gd:BVO films on FTO substrates showing reduced porosity with Gd doping. Scale bars for top- and side-view SEMs are 200 and 500 nm, respectively. (b) XRD spectra for bare BVO and BVO with various Gd doping concentrations showing a phase transition from monoclinic scheelite to tetragonal scheelite. (c) XPS spectra for bare BVO (black) and 6% Gd:BVO (red) in the oxygen 1s, vanadium 2p, bismuth 4f, and Gd 4d binding energy regions.

surface Bi atoms on these facets are the dominant adsorption site for the intermediates (see Supporting Information Figure S1). The  $\Delta G_{\text{OH}^*}$  values over (001), (011), and (101) are found to be 2.85, 2.65, and 2.60 eV (Figure 1b, right red zone), respectively, indicating that these facets are more prone to produce OH radical rather than  $\text{H}_2\text{O}_2$ . However, the (111) facet can have several different termination patterns (see Supporting Information Figure S2). For each termination pattern, there are two Bi–Bi bridges (with different surface orientations) that serve as active sites (Figure 1a). DFT optimization of the (111) facets shows that the two bridges are slightly different in terms of Bi–Bi interatomic distances and the interactions with nearby  $\text{VO}_4$  units; therefore, they may present different adsorption properties for reaction intermediates. Indeed, the calculated  $\Delta G_{\text{OH}^*}$  for different possible termination patterns of the (111) facet vary from 1.87 to 2.05 eV when considering all possible Bi–Bi bridges (Table S1). Nevertheless, these results clearly indicate that for undoped  $\text{BiVO}_4$  only the (111) facet favors  $\text{H}_2\text{O}_2$  production over other water oxidation reactions (Figure 1b).

Next, we examine Gd-doped  $\text{BiVO}_4$ , where Gd substitutes for a surface Bi atom in our slab models (i.e.,  $\text{Gd}_x\text{Bi}_{1-x}\text{VO}_4$ ).

We calculate the adsorption energy of the reaction intermediates on all possible surfaces constructed from replacing either one or two surface Bi sites with Gd. For the (001), (011), and (101) facets, modeling the Gd atom as the active site, a low concentration of Gd doping (replacing a surface Bi with Gd, denoted LGd) reduces the  $\Delta G_{\text{OH}^*}$  value (Figure 1b, from red to green points). Our results indicate that the (011) and (101) facets, when doped with Gd, move into the region favoring  $\text{H}_2\text{O}_2$  production (Figure 1b, middle green zone). For the (111) facet, Bi–Gd bridges become additional active sites. Table S1 (see the Supporting Information) summarizes the calculated  $\Delta G_{\text{OH}^*}$  values of all of the possible Gd–Bi bridges over different termination patterns for the (111) facet (also see Supporting Information Figure S3). With low concentrations of Gd doping, almost all Gd–Bi bridges have more suitable  $\Delta G_{\text{OH}^*}$  values for  $\text{H}_2\text{O}_2$  than those of the corresponding Bi–Bi bridges. The optimal Gd–Bi bridge has a  $\Delta G_{\text{OH}^*}$  value of 1.75 eV, very close to the desired 1.76 eV. When the Gd doping concentration is high (denoted HGD), both Bi atoms of the Bi–Bi bridge sites of the (111) facet are replaced with Gd atoms (see Supporting Information Figure S4). Such a change leads to overstrengthening of the binding

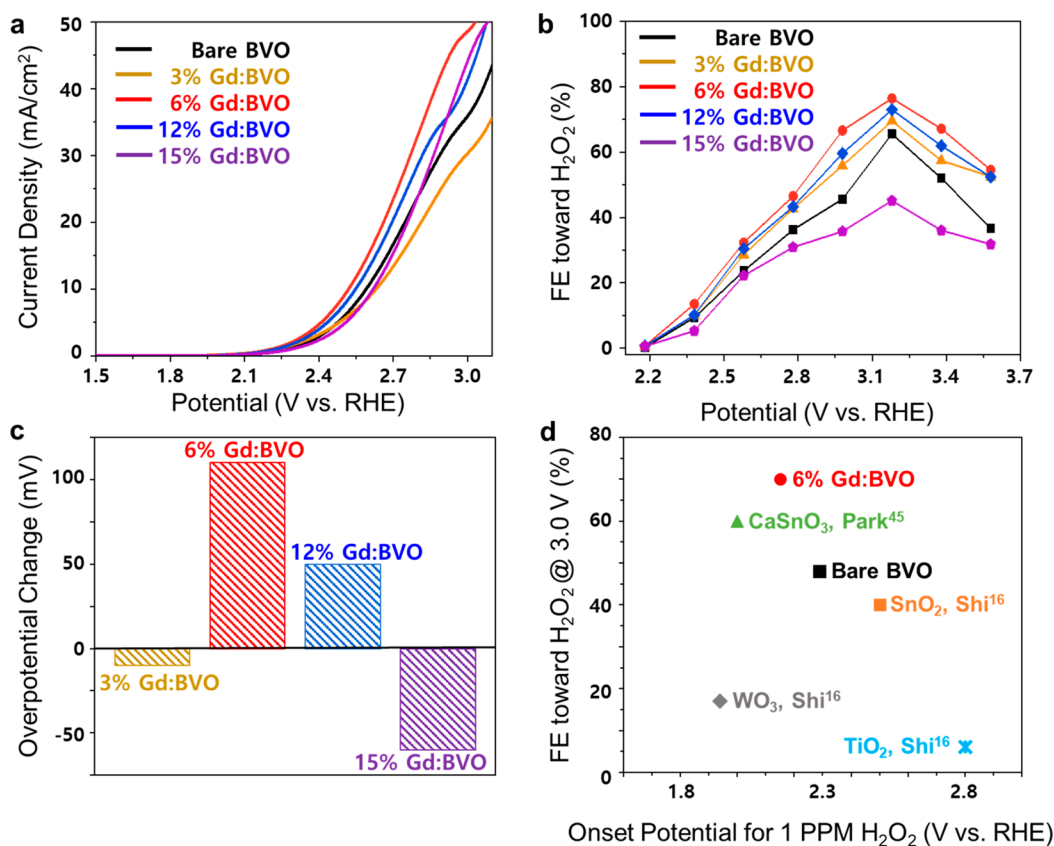


**Figure 3.** Electrochemical performance for H<sub>2</sub>O<sub>2</sub> production in dark conditions. (a) Current density vs potential curves for BVO with various Gd doping concentrations and 20 nm thickness under dark conditions. (b) FE measurements collected over 5 min at various constant applied potentials for several Gd doping concentrations under dark conditions. (c) Overpotential change (relative to bare BiVO<sub>4</sub>, which has an overpotential of 1270 mV according to this metric) for various doping concentrations, defined as the voltage beyond 1.76 V vs RHE necessary to generate a H<sub>2</sub>O<sub>2</sub> current density of 5 mA/cm<sup>2</sup>. (d) Comparison of the onset potential and FE toward H<sub>2</sub>O<sub>2</sub> measured at 3.0 V vs RHE for Gd:BVO and several other metal oxides benchmarked in the literature.<sup>16,45</sup> All experiments were conducted under dark conditions in 2 M potassium bicarbonate electrolyte.

of OH\* ( $\Delta G_{\text{OH}^*} = 1.35$  eV), pushing the selectivity toward the four-electron oxygen evolution reaction (reaction R2) on the left side of the volcano plot (Figure 1b, compare yellow with red and green points). In addition, we calculate  $\Delta G_{\text{OH}^*}$  of various Gd-doped BiVO<sub>4</sub>, assuming that a surface Bi atom adsorbs OH and a nearby Bi atom (either at the first or second layer) is replaced with Gd (see Supporting Information Figure S5). We find that Gd has little impact on the  $\Delta G_{\text{OH}^*}$  of neighboring Bi sites, suggesting that Gd needs to participate in binding the intermediates to influence the activity toward H<sub>2</sub>O<sub>2</sub> production. These theoretical results establish that doping of the BiVO<sub>4</sub> with Gd at an optimum concentration decreases the overpotential for H<sub>2</sub>O<sub>2</sub> production (Figure 1c).

Next, we further examine the effect of Gd doping on the stability of BiVO<sub>4</sub>. The atomic partial charges of the studied facets are estimated by Bader charge analysis.<sup>31–33</sup> This analysis indicates that the Gd atoms doped at the surface of BiVO<sub>4</sub> are more positively charged ( $q$ ) than Bi, in agreement with the lower electronegativity of Gd than that of Bi.<sup>34</sup> For example,  $q_{\text{Bi}}$  and  $q_{\text{Gd}}$  of BiVO<sub>4</sub> and Gd<sub>*x*</sub>Bi<sub>1–*x*</sub>VO<sub>4</sub>(111) are found to be about +1.96 and +2.16  $e$ , respectively. The replacement of a Bi atom with Gd leads to a more negative charge of  $\sim -0.05$   $e$  on neighboring oxygen atoms, making the nearby VO<sub>4</sub> units more negatively charged. In other words, Gd has a stronger electrostatic interaction with the VO<sub>4</sub> units in the lattice than does Bi. Consequently, this may cause the

removal of surface VO<sub>4</sub> units from the catalyst to be less favorable. To further evaluate this, we performed single-point DFT calculations for BiVO<sub>4</sub>(001) and Gd<sub>*x*</sub>Bi<sub>1–*x*</sub>VO<sub>4</sub>(001) systems after a surface VO<sub>4</sub> was removed. Such calculations provide an estimate of the relative bonding energy of VO<sub>4</sub> within the two given systems. DFT predicts that the removal of a surface VO<sub>4</sub> from the Gd<sub>*x*</sub>Bi<sub>1–*x*</sub>VO<sub>4</sub>(001) is  $\sim 0.65$  eV endothermic relative to the undoped BiVO<sub>4</sub>(001) system, viz., VO<sub>4</sub> units experience a more favorable bonding energy within Gd<sub>*x*</sub>Bi<sub>1–*x*</sub>VO<sub>4</sub>(001) than those within BiVO<sub>4</sub>(001). Because the dissolution of surface VO<sub>4</sub> is a key mechanism for BiVO<sub>4</sub> degradation, the strengthening of its binding via Gd doping should slow down this process and improve the stability of BiVO<sub>4</sub>.

We briefly pause here for perspective. The theoretical results presented above reveal that doping BiVO<sub>4</sub> with Gd can generally result in a moderately stronger interaction of oxygen species (e.g., OH\*, O\*, and VO<sub>4</sub>) at the surface, offering a potential method for achieving higher activity and stability of the catalyst for H<sub>2</sub>O<sub>2</sub> synthesis. While our DFT study reported here contributes novel insights on the promotional effect of Gd atoms on the electrochemical synthesis of H<sub>2</sub>O<sub>2</sub>, some aspects are not properly accounted for in our analysis due to high computational expenses. As the Gd concentration is increased, a gradual structural deformation of the host BiVO<sub>4</sub>, resulting in a phase change, is possible. It would be worthwhile in the

future to extend the current DFT study to track possible local changes in the crystal phase of  $\text{BiVO}_4$  with high concentrations of Gd and the effects that these changes have on the electrochemical activity of the catalyst surface.

**Characterization of Gd-Doped  $\text{BiVO}_4$  Photoanode.** To verify the theoretical results elucidated above,  $\text{BiVO}_4$  (BVO) films with Gd doping concentrations ranging from 0 atom % (Bi:Gd:V = 1:0:1) to 15 atom % (Bi:Gd:V = 0.85:0.15:1) were synthesized on fluorine-doped tin oxide (FTO) substrates via a spin-coating and annealing procedure (see the Methods section in the Supporting Information for details). Regarding notation, either bare or undoped BVO is used for samples without Gd, and X% Gd:BVO is used for Gd-doped samples, where X is the atomic percentage of Gd salt substituted for Bi salt in the precursor solution. The side-view SEM images in Figure 2a show that the as-prepared BVO and 6% Gd:BVO films are uniformly distributed on FTO. Though difficult to discern in the side-view image, only the top  $\sim 100$  nm of the sample consists of deposited material,<sup>25</sup> while the underlying uneven surface is the FTO substrate. The top-view SEM images show that 6% Gd:BVO is significantly less porous than the bare BVO sample, a trend that extends to all Gd doping concentrations in this study (Figure S6). This trend may be due to the tendency of Gd to bind surface oxygen, thereby closing surface pores, a phenomenon observed with other oxyphilic lanthanide metal dopants.<sup>35</sup>

Figure 2b shows the XRD spectra for BVO with various amounts of Gd dopant. In general, BVO forms three prominent crystal structures: monoclinic scheelite, tetragonal scheelite, and tetragonal zircon.<sup>36</sup> Among them, the crystal structure of tetragonal scheelite BVO is analogous to monoclinic scheelite BVO, but with a greater degree of distortion of the Bi–O polyhedra due to the interaction with the  $6s^2$  lone pair of the  $\text{Bi}^{3+}$  ions. Thus, the tetragonal scheelite BVO can generally change phase from monoclinic scheelite to tetragonal scheelite under heating. In this study, for bare BVO and low Gd doping concentrations (1% Gd:BVO), the peaks in the XRD data match with the monoclinic scheelite BVO spectra (JCPDS #14-0688). As the Gd doping concentration increases, the monoclinic bimodal peak near  $2\theta = 35^\circ$  (highlighted) becomes a single peak, indicating that the BVO structure shifts from the monoclinic scheelite to the tetragonal scheelite phase (JCPDS #10-5710). This is also supported by the shifting of the  $2\theta = 60^\circ$  peak to nearly unimodal with increasing Gd doping concentrations. Similar results of this phase shift have been observed and detailed in previous reports.<sup>36,37</sup> This shift was also shown to improve light absorption<sup>37,38</sup> and the electrical conductivity of BVO,<sup>39</sup> though conflicting reports of these effects exist in the literature.<sup>40</sup>

The surface chemical states of undoped BVO (black) and 6% Gd:BVO (red) are further analyzed by XPS. Figure 2c shows the O 1s, V 2p, Bi 4f, and Gd 4d XPS spectra. For the O 1s peaks, both samples exhibit strong peaks at binding energies near 530 eV, corresponding with the oxygen binding energy in BVO.<sup>41</sup> For the V 2p region, the two peaks at 524.8 and 516.7 eV correlate with the V  $2p_{1/2}$  and  $2p_{3/2}$  binding energies in BVO, respectively.<sup>41</sup> The Bi 4f peaks at 163.3 and 159.1 eV also match with reported BVO well.<sup>41,42</sup> The slight shift in O 1s and Bi 4f binding energy upon doping may be attributable to the oxophilicity of Gd, as will be discussed later. Finally, the Gd 4d spectra exhibit peaks near 148 and 142 eV, matching well with the  $4d_{3/2}$  and  $4d_{5/2}$  binding energies for Gd in

$\text{Gd}_2\text{O}_3$ <sup>43</sup> and further implicating Gd binding to oxygen upon doping.<sup>43</sup> The XPS results indicate successful incorporation of Gd in BVO for the 6% Gd:BVO.

**Electrochemical Performance under Dark Conditions.** The electrocatalytic performance of BVO thin films ( $\sim 20$  nm) with various amounts of Gd doping (0–15%) was first evaluated under dark conditions, with Figure 3a showing the corresponding current–voltage curves. Intermediate Gd doping concentrations enhance both the onset and the current density under dark conditions, where 6% Gd:BVO shows  $>40\%$  improvement in overall current density at 3.0 V vs RHE. Low (i.e., 3%) and high (i.e., 15%) concentrations of the Gd dopant are seen to maintain or degrade the electrochemical performance of the undoped sample, in agreement with our DFT results (Figure 1b), which suggest that an optimal, intermediate amount of Gd doping is needed to enhance BVO activity toward  $\text{H}_2\text{O}_2$ .

The selectivity of the various Gd:BVO samples was investigated by measuring the FE for  $\text{H}_2\text{O}_2$  as a function of applied potential. Figure 3b shows that the FE for  $\text{H}_2\text{O}_2$  is maximized near 3.2 V vs RHE under dark conditions for all Gd:BVO samples. The 6% Gd:BVO exhibits the highest peak FE of 78%, which is higher than that of undoped BVO ( $\sim 64\%$ ). At very high Gd concentrations, such as 15% Gd:BVO, the peak FE falls to  $\sim 45\%$ . This trend agrees well with our theoretical predictions (Figure 1b), which show that high concentrations of Gd dopant push the  $\text{OH}^*$  binding energy into the oxygen evolution regime, thereby reducing the selectivity toward hydrogen peroxide.

Oxygen generation (the suspected secondary product) was detected qualitatively with an oxygen probe, and the FE toward oxygen generation was quantified in a sealed electrochemical system using gas chromatography (Figure S7). The results show that oxygen is in fact the other water oxidation product being formed and that the FE toward oxygen generation measured using chromatography is commensurate with the measured FE toward  $\text{H}_2\text{O}_2$ . Furthermore, the rate of  $\text{H}_2\text{O}_2$  generation per unit area is plotted in Figure S8, which shows a dependence on the Gd concentration that is similar to that seen in the FE measurements. The  $\text{H}_2\text{O}_2$  production rates per geometric electrode area for all BVO samples reach a plateau beyond  $\sim 3.2$  V, and bubbles are clearly seen on the electrode surface at higher applied bias. This suggests that when high bias is applied both oxygen evolution and  $\text{H}_2\text{O}_2$  proceed more quickly and  $\text{O}_2$  is preferentially evolved. In other words, the preferred production of  $\text{H}_2\text{O}_2$  lies in a narrow, intermediate bias range (1.9–3.2 V vs RHE) under dark conditions.

For a clearer comparison of activity among dopant concentrations, the change in overpotential (relative to undoped  $\text{BiVO}_4$ ), defined as the voltage beyond 1.76 V vs RHE necessary to generate a  $\text{H}_2\text{O}_2$  current density of 5 mA/ $\text{cm}^2$ , is shown in Figure 3c. Here, the  $\text{H}_2\text{O}_2$  current density is defined as  $J_{\text{H}_2\text{O}_2} = J_{\text{Total}} \times \text{FE}_{\text{H}_2\text{O}_2}$ . The trend again shows that intermediate doping concentrations such as 6% can reduce the overpotential for  $\text{H}_2\text{O}_2$  by as much as 110 mV, suggesting substantially enhanced activity.

Electrochemical impedance spectroscopy measurements were conducted to further verify the mechanism for improvement in electrochemical performance (i.e., intrinsic activity enhancement, electrical conductivity increase, etc.) in the doped water oxidation electrode system (Figure S9). Notably, the charge transfer resistance between the electrode surface and the electrolyte is reduced to 1/3 of the undoped value after

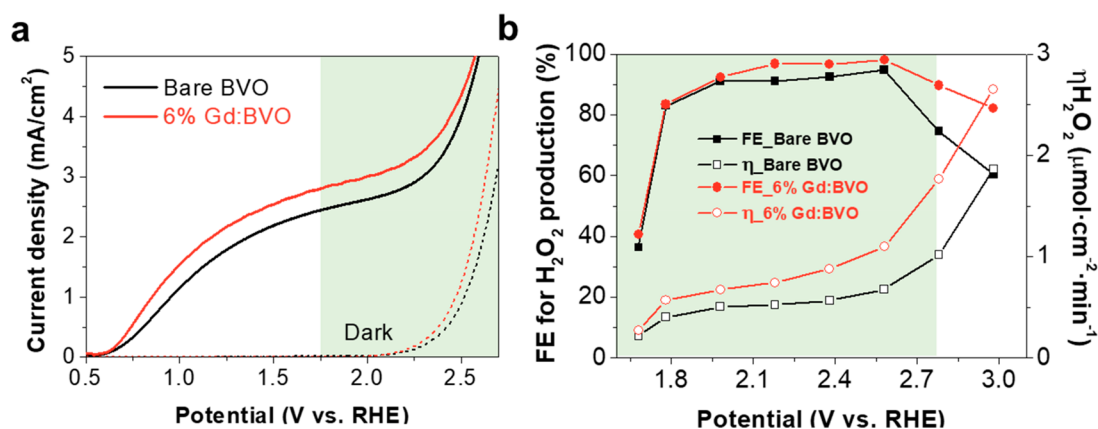


Figure 4. Photoelectrochemical production of H<sub>2</sub>O<sub>2</sub> under illumination. (a) Current density vs potential curves for undoped and 6% Gd-doped BVO thick films (~100 nm) under 1 sun illumination. (b) FE measurements and hydrogen peroxide generation rate collected over 5 min at various constant applied potentials under 1 sun illumination. All measurements were conducted in 2 M potassium bicarbonate electrolyte.

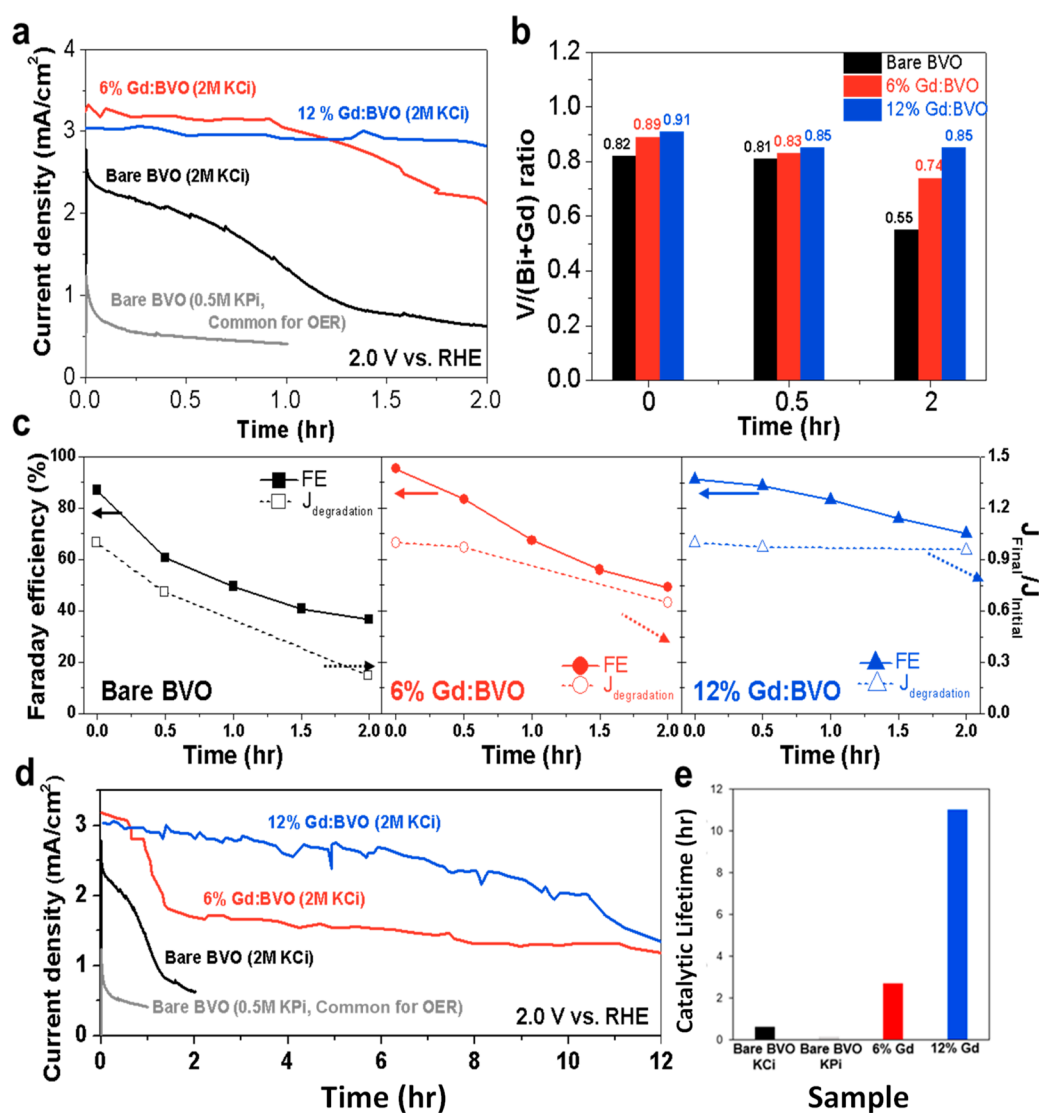


Figure 5. Stability of Gd-doped BVO for H<sub>2</sub>O<sub>2</sub> production under illumination. (a) The 2 h stability test for 12% Gd:BVO (blue), 6% Gd:BVO (red), and bare BVO (black) in 2 M KCl electrolyte and bare BVO in 0.5 M KPi electrolyte (gray) at 2.0 V vs RHE under 1 sun illumination. (b) Ratio of vanadium to bismuth and gadolinium as measured by XPS over the course of the 2 h stability test. (c) Current density degradation and FE as a function of time in 2 M KCl electrolyte (solid line: FE; dotted line: current density degradation). (d) Extended stability test at 2.0 V vs RHE under 1 sun illumination. (e) Comparison of catalytic lifetime after extended stability test.

6% doping, indicating a strong enhancement of material activity for water oxidation.<sup>44</sup>

Finally, the FE and onset potential of the Gd-doped BVO compare very favorably with those of previously studied metal oxides (Figure 3d).<sup>16,45</sup> Here, the onset potential is defined as described in previous H<sub>2</sub>O<sub>2</sub> studies: the bias necessary to establish a concentration of 1 ppm of H<sub>2</sub>O<sub>2</sub> in a 10 min potentiostatic test in 20 mL of electrolyte using a 1 cm<sup>2</sup> sample. The onset potential (2.15 V for 6% Gd:BVO) is relatively competitive with even the most active known metal oxides (i.e., WO<sub>3</sub> at 1.93 V), while the selectivity toward H<sub>2</sub>O<sub>2</sub> is more than 3-fold better (70 vs <20%). Accordingly, the electrochemical performance of the Gd:BVO is among the highest for four-electron water oxidation.

**Photoelectrochemical Performance toward H<sub>2</sub>O<sub>2</sub> under Illumination.** The above dark *J*–*V* characterization shows that 6% Gd doping improves the catalytic activity and selectivity of bare BVO toward H<sub>2</sub>O<sub>2</sub>. We further evaluated the effect of 6% Gd doping on the H<sub>2</sub>O<sub>2</sub> production performance under 1 sun illumination. It should be noted that the BVO films (~100 nm) used for PEC characterization are much thicker than the films (~20 nm) discussed above for electrochemical studies because thicker films are needed to effectively absorb sunlight. Figure S10 shows the detailed film thickness optimization for balancing light absorption and charge transfer processes. Figure 4a shows the current density–voltage characteristics of the bare BVO and 6% Gd:BVO film with optimal thickness (~100 nm, Figure 2a) under light (solid lines) and dark (dash lines), and Figure 4b compares their corresponding FEs and H<sub>2</sub>O<sub>2</sub> production rates for the shaded potential range in Figure 4a. Clearly, illumination effectively shifts the current onset potential from ~2.0 (dark) to ~0.6 V vs RHE (Figure 4a). The 6% Gd:BVO sample shows an earlier current onset, higher current density, and higher FE and production rate of H<sub>2</sub>O<sub>2</sub> than does bare BVO, confirming the benefits of Gd doping. Illumination also increases the peak FE for H<sub>2</sub>O<sub>2</sub> from 81% at 3.2 V to nearly 100% at 2.6 V vs RHE for 6% Gd:BVO, which is partially due to the enhanced conductance of BVO under illumination (Figures 3c and 4b). Generally, 6% Gd:BVO achieves a FE toward H<sub>2</sub>O<sub>2</sub> of over 80% for a wide potential range of 1.8–3.0 V vs RHE, suggesting the viability of 6% Gd:BVO as a photoanode for H<sub>2</sub>O<sub>2</sub> production.

**Stability for H<sub>2</sub>O<sub>2</sub> Production under Illumination.** BVO is known to be an unstable photoanode, attributable to dissolution of vanadium and/or the vanadate ion into the electrolyte.<sup>25,26,46–48</sup> Hence, we further tested the effect of Gd doping on the stability of BVO by comparing bare BVO, 6% Gd:BVO, and 12% Gd:BVO using chronoamperometry (Figure 5a–d; *J*–*V* curves: Figure S11). Due to the relatively high thermodynamic potential required to produce H<sub>2</sub>O<sub>2</sub> and the known photocorrosion issues associated with BVO,<sup>24–26,46</sup> these tests were conducted both at high bias (~2.0 V vs RHE) and under 1 sun illumination to simulate in operando conditions. Moreover, as a stability comparison, a bare BVO sample was tested under the same harsh conditions in a typical oxygen evolution electrolyte, 0.5 M potassium phosphate (abbreviated as KPi), instead of the 2 M potassium bicarbonate (abbreviated as KCi) electrolyte, which is favorable for H<sub>2</sub>O<sub>2</sub> production.<sup>16,49</sup> First, the bare BVO deteriorates within 0.5 h for the OER electrolyte 0.5 M KPi and lasts just a few minutes longer under the H<sub>2</sub>O<sub>2</sub> favorable electrolyte 2 M KCi (Figure 4a). Second, comparing the

samples tested in 2 M KCi shows that Gd doping clearly improves the stability as the 12% Gd:BVO exhibits a more sustained photocurrent density than does 6% Gd:BVO (Figure 4a). To confirm that Gd slows down the dissolution of V, we measured the vanadium fraction (V/(Gd+Bi)) before testing, at 0.5 h and after 2 h of PEC testing using XPS analysis (Figure 5b; see Figure S12 for detailed progression), which clearly shows that the surface V fraction drops about 6% (=91–85%) for 12% Gd:BVO as compared to 27% (=82–55%) for bare BVO after 2 h. Figure 5c plots the detailed FE and normalized current density as a function of time for these three samples. For all three samples, the degradation in current density over time correlates strongly with the reduction in V fraction (Figure 5b,c). As the V dissolves and current density decreases, the FE for H<sub>2</sub>O<sub>2</sub> also drops. Nevertheless, Gd doping clearly improves the overall stability of BVO. The enhanced stability agrees with the DFT results in that Gd increases the dissolution energy of VO<sub>4</sub><sup>3–</sup> by 0.65 eV. This is due to the stronger electrostatic interaction between Gd and VO<sub>4</sub> in the BVO lattice and the structural change to tetragonal scheelite shown in the XRD analysis (Figure 3b).<sup>26</sup>

Finally, similar trends are observed in longer term (12 h) stability tests (Figure 5d). Interestingly, whereas the 6% Gd:BVO and bare BVO samples exhibit an initial precipitous decline in current density followed by a plateau, the 12% Gd:BVO sample seems to degrade more steadily over the 12 h period. This may be the result of different intermediate states being formed as vanadium is dissolved depending on the amount of Gd, but further probing is beyond the scope of this study. Holistically, the catalytic lifetime, defined as the time for the photocurrent density to be halved from its initial value, is increased from ~30 min for bare BVO to ~11.5 h for 12% Gd:BVO (Figure 5e), indicating a drastic improvement in stability.

Our combined DFT calculations and experiments demonstrate that doping bismuth vanadate with moderate amounts of Gd simultaneously increases its activity, selectivity, and stability for the two-electron water oxidation reaction to produce H<sub>2</sub>O<sub>2</sub>. Under the optimal Gd doping concentration, the overpotential for H<sub>2</sub>O<sub>2</sub> production is reduced by ~110 mV under dark conditions. The selectivity of BiVO<sub>4</sub> is improved from 64% in undoped BVO to 78% in 6% Gd:BVO at 3.1 V vs RHE under dark conditions. The activity and selectivity enhancement come from several synergetic effects. First, moderate amounts of Gd doping move the OH binding energy on the existing active sites (Bi–Bi) closer to the optimal energy level. In addition, the presence of Gd introduces additional active sites for H<sub>2</sub>O<sub>2</sub> production, such as Gd–Gd and Gd–Bi bridges. Under illumination, 6% Gd:BVO reaches a peak FE of ~99.5% for H<sub>2</sub>O<sub>2</sub> production and exceeds 80% for a wide potential range of 1.8–3.0 V vs RHE, proving that Gd:BiVO<sub>4</sub> is a great photoanode for producing H<sub>2</sub>O<sub>2</sub>. Importantly, even under high applied bias (2.0 V vs RHE) and under illumination, the catalytic lifetime of BVO is increased from ~30 min for bare BVO to ~11.5 h for 12% Gd:BVO, a 22-fold increase. The stabilization effect of Gd results from its enhanced electrostatic interactions with lattice ions. Our results suggest that the use of rare earth element doping is an effective method to simultaneously tune the catalyst's activity, selectivity, and stability. Our 6% Gd:BVO photoanodes can be further improved using other dopants and nanostructured catalyst materials and by integrating heterojunctions, therein providing further opportunity for new

catalytic research on production of a valuable resource in  $\text{H}_2\text{O}_2$ .

## ■ ASSOCIATED CONTENT

### Supporting Information

The Supporting Information is available free of charge on the ACS Publications website at DOI: 10.1021/acseenergylett.9b00277.

Detailed information on experimental and computational methods, DFT calculations, SEM images of Gd-doped  $\text{BiVO}_4$  photoanodes, potentiostatic rate of  $\text{H}_2\text{O}_2$  production for Gd-doped  $\text{BiVO}_4$  photoanodes, thickness optimization, and total element quantification of the samples (PDF)

## ■ AUTHOR INFORMATION

### Corresponding Authors

\*E-mail: [hsjung1@skku.edu](mailto:hsjung1@skku.edu).

\*E-mail: [samiras.siahrostami@ucalgary.ca](mailto:samiras.siahrostami@ucalgary.ca).

\*E-mail: [xlzheng@stanford.edu](mailto:xlzheng@stanford.edu).

### ORCID

Hadi Abroshan: 0000-0003-1046-5170

Hyun Suk Jung: 0000-0002-7803-6930

Samira Siahrostami: 0000-0002-1192-4634

Xiaolin Zheng: 0000-0002-8889-7873

### Author Contributions

<sup>†</sup>J.H.B., T.M.G., and X.S. fabricated the devices and performed electrochemical measurements. H.A. and S.S. calculated and analyzed the theoretical data. S.P. and J.H.B. conducted materials characterizations. J.H.B., T.M.G., and H.A. conceived of the experiment and wrote the manuscript. H.S.J., J.N., S.S., and X.Z. directed the research. All authors read the manuscript and provided comments. J.H.B., T.M.G., and H.A. contributed equally to this work.

### Notes

The authors declare no competing financial interest.

## ■ ACKNOWLEDGMENTS

This work was supported by the Basic Science Research Program through the National Research Foundation of Korea (No. 2017R1A2B3010927), the Global Frontier R&D Program of the Center for Multiscale Energy System (2012M3A6A7054855), and the Creative Materials Discovery Program (2016M3D1A1027664).

## ■ REFERENCES

- (1) Campos-Martin, J. M.; Blanco-Brieva, G.; Fierro, J. L. G. Hydrogen Peroxide Synthesis: An Outlook Beyond the Anthraquinone Process. *Angew. Chem., Int. Ed.* **2006**, *45*, 6962–6984.
- (2) Liu, N.; Han, M.; Sun, Y.; Zhu, C.; Zhou, Y.; Zhang, Y.; Huang, H.; Kremnican, V.; Liu, Y.; Lifshitz, Y.; Kang, Z. Ag-C<sub>3</sub>N<sub>4</sub> Based Photoelectrochemical Cell Using O<sub>2</sub>/H<sub>2</sub>O Redox Couples. *Energy Environ. Sci.* **2018**, *11*, 1841–1847.
- (3) Chen, Z.; Chen, S. C.; Siahrostami, S.; Chakthranont, P.; Hahn, C.; Nordlund, D.; Dimosthenis, S.; Norskov, J. K.; Bao, Z.; Jaramillo, T. Development of a Reactor with Carbon Catalysts for Modular-Scale, Low-Cost Electrochemical Generation of H<sub>2</sub>O<sub>2</sub>. *React. Chem. Eng.* **2017**, *2*, 239–245.
- (4) Shi, X.; Zhang, Y.; Siahrostami, S.; Zheng, X. Light-Driven BiVO<sub>4</sub>-C Fuel Cell with Simultaneous Production of H<sub>2</sub>O<sub>2</sub>. *Adv. Energy Mater.* **2018**, *8*, 1801158–1801167.

- (5) Ando, Y.; Tanaka, T. Proposal for a New System for Simultaneous Production of Hydrogen and Hydrogen Peroxide by Water Electrolysis. *Int. J. Hydrogen Energy* **2004**, *29*, 1349–1354.
- (6) Izgorodin, A.; Izgorodina, E.; MacFarlane, D. R. Low Overpotential Water Oxidation to Hydrogen Peroxide on a MnOx Catalyst. *Energy Environ. Sci.* **2012**, *5*, 9496–9501.
- (7) Izgorodin, A.; MacFarlane, D.R. Australian Patent Office, 2012905597, 2012.
- (8) Siahrostami, S.; Li, G. L.; Viswanathan, V.; Norskov, J. K. One- or Two-Electron Water Oxidation, Hydroxyl Radical, or H<sub>2</sub>O<sub>2</sub> Evolution. *J. Phys. Chem. Lett.* **2017**, *8*, 1157–1160.
- (9) Bard, A. J.; Parsons, R.; Jordan, J. *Standard Potentials in Aqueous Solutions*; CRC Press: New York, 1985.
- (10) McDonnell-Worth, C.; Macfarlane, D. R. Ion Effects in Water Oxidation to Hydrogen Peroxide. *RSC Adv.* **2014**, *4*, 30551–30557.
- (11) Fuku, K.; Sayama, K. Efficient Oxidative Hydrogen Peroxide Production and Accumulation in Photoelectrochemical Water Splitting Using a Tungsten Trioxide/Bismuth Vanadate Photoanode. *Chem. Commun.* **2016**, *52*, 5406–5409.
- (12) Mase, K.; Yoneda, M.; Yamada, Y.; Fukuzumi, S. Efficient Photocatalytic Reduction of Hydrogen Peroxide from Water and Dioxygen with Bismuth Vanadate and a Cobalt(II) Chlorin Complex. *ACS Energy Lett.* **2016**, *1*, 913–919.
- (13) Fuku, K.; Miyase, Y.; Miseki, Y.; Gunji, T.; Sayama, K. Enhanced Oxidative Hydrogen Peroxide Production on Conducting Glass Anodes Modified with Metal Oxides. *ChemistrySelect* **2016**, *1*, 5721–5726.
- (14) Hirakawa, T.; Yawata, K.; Nosaka, Y. Photocatalytic Reactivity for O<sub>2</sub>\*- and OH\* Radical Formation in Anatase and Rutile TiO<sub>2</sub> Suspension as the Effect of H<sub>2</sub>O<sub>2</sub> Addition. *Appl. Catal., A* **2007**, *325*, 105–111.
- (15) Goto, H.; Hanada, Y.; Ohno, T.; Matsumura, M. Quantitative Analysis of Superoxide Ion and Hydrogen Peroxide Produced from Molecular Oxygen on Photoirradiated TiO<sub>2</sub> Particles. *J. Catal.* **2004**, *225*, 223–229.
- (16) Shi, X.; Siahrostami, S.; Li, G.-L.; Zhang, Y.; Chakthranont, P.; Studt, F.; Jaramillo, T. F.; Zheng, X.; Norskov, J. K. Understanding Activity Trends in Electrochemical Water Oxidation to Form Hydrogen Peroxide. *Nat. Commun.* **2017**, *8*, 701–707.
- (17) Park, Y.; McDonald, K. J.; Choi, K.-S. Progress in Bismuth Vanadate Photoanodes for Use in Solar Water Oxidation. *Chem. Soc. Rev.* **2013**, *42*, 2321–2337.
- (18) Han, H. S.; Shin, S.; Kim, D. H.; Park, I. J.; Kim, J. S.; Huang, P.-S.; Lee, J.-K.; Cho, I. S.; Zheng, X. Boosting Solar Water Oxidation Performance of BiVO<sub>4</sub> Photoanode by Crystallographic Orientation Control. *Energy Environ. Sci.* **2018**, *11*, 1299–1306.
- (19) Guevarra, D.; Shinde, A.; Suram, S. K.; Sharp, I. D.; Toma, F. M.; Haber, J. A.; Gregoire, J. M. Development of Solar Fuels Photoanodes Through Combinatorial Integration of Ni–La–Co–Ce Oxide Catalysts on BiVO<sub>4</sub>. *Energy Environ. Sci.* **2016**, *9*, 565–580.
- (20) Tong, L.; Iwase, A.; Nattestad, A.; Bach, U.; Weidener, M.; Götz, G.; Mishra, A.; Bäuerle, P.; Amal, R.; Wallace, G. G.; Mozer, A. J. Sustained Solar Hydrogen Generation Using a Dye-Sensitized NiO Photocathode/BiVO<sub>4</sub> Tandem Photo-Electrochemical Device. *Energy Environ. Sci.* **2012**, *5*, 9472–9475.
- (21) Luo, W.; Yang, Z.; Li, Z.; Zhang, J.; Liu, J.; Zhao, Z.; Wang, Z.; Yan, S.; Yu, T.; Zou, Z. Solar Hydrogen Generation from Seawater with a Modified BiVO<sub>4</sub> Photoanode. *Energy Environ. Sci.* **2011**, *4*, 4046–4051.
- (22) Ye, K.-H.; Wang, Z.; Gu, J.; Xiao, S.; Yuan, Y.; Zhu, Y.; Zhang, Y.; Mai, W.; Yang, S. Carbon Quantum Dots as a Visible Light Sensitizer to Significantly Increase the Solar Water Splitting Performance of Bismuth Vanadate Photoanodes. *Energy Environ. Sci.* **2017**, *10*, 772–779.
- (23) Pili, S. K.; Furtak, T. E.; Brown, L. D.; Deutsch, T. G.; Turner, J. A.; Herring, A. M. Cobalt-Phosphate (Co-Pi) Catalyst Modified Mo-doped BiVO<sub>4</sub> Photoelectrodes for Solar Water Oxidation. *Energy Environ. Sci.* **2011**, *4*, 5028–5034.

- (24) McDowell, M. T.; Lichterman, M. F.; Spurgeon, J. M.; Hu, S.; Sharp, I. D.; Brunschwig, B. S.; Lewis, N. S. Improved Stability of Polycrystalline Bismuth Vanadate Photoanodes by use of Dual-Layer Thin  $\text{TiO}_2/\text{Ni}$  Coatings. *J. Phys. Chem. C* **2014**, *118*, 19618–19624.
- (25) Toma, F. M.; Cooper, J. K.; Kunzelmann, V.; McDowell, M. T.; Yu, J.; Larson, D. M.; Borys, N. J.; Abelyan, C.; Beeman, J. W.; et al. Mechanistic Insights into Chemical and Photochemical Transformations of Bismuth Vanadate Photoanodes. *Nat. Commun.* **2016**, *7*, 12012–12023.
- (26) Abdi, F. F.; Firet, N.; Dabirian, A.; van de Krol, R. Spray-deposited Co-Pi Catalyzed  $\text{BiVO}_4$ : A Low-cost Route Towards Highly Efficient Photoanodes. *MRS Online Proc. Libr.* **2012**, *1446*, 7–12.
- (27) Dehnicke, K.; Greiner, A. Unusual Complex Chemistry of Rare-earth Elements: Large Ionic Radii—Small Coordination Numbers. *Angew. Chem., Int. Ed.* **2003**, *42*, 1340–1354.
- (28) Kepp, K. P. A Quantitative Scale of Oxophilicity and Thiophilicity. *Inorg. Chem.* **2016**, *55*, 9461–9470.
- (29) Viswanathan, V.; Hansen, H. A.; Nørskov, J. K. Selective Electrochemical Generation of Hydrogen Peroxide from Water Oxidation. *J. Phys. Chem. Lett.* **2015**, *6*, 4224–4228.
- (30) Man, I. C.; Su, H.-Y.; Calle-Vallejo, F.; Hansen, H. A.; Martínez, J. I.; Inoglu, N. G.; Kitchin, J.; Jaramillo, T. F.; Nørskov, J. K.; Rossmeisl, J. Universality in Oxygen Evolution Electrocatalysis on Oxide Surfaces. *ChemCatChem* **2011**, *3*, 1159–1165.
- (31) Sanville, E.; Kenny, S. D.; Smith, R.; Henkelman, G. Improved Grid-based Algorithm for Bader Charge Allocation. *J. Comput. Chem.* **2007**, *28*, 899–908.
- (32) Henkelman, G.; Arnaldsson, A.; Jónsson, H. A Fast and Robust Algorithm for Bader Decomposition of Charge Density. *Comput. Mater. Sci.* **2006**, *36*, 354–360.
- (33) Tang, W.; Sanville, E.; Henkelman, G. A Grid-based Bader Analysis Algorithm Without Lattice Bias. *J. Phys.: Condens. Matter* **2009**, *21*, 084204–084211.
- (34) Emsley, J. *The Elements*, 3rd ed.; Clarendon Press: Oxford, U.K., 1998.
- (35) Mula, G.; Printemps, T.; Licitra, C.; Sogne, E.; D'Acapito, F.; Gambacorti, N.; Sestu, N.; Saba, M.; Pinna, E.; Chiriu, D.; et al. Doping Porous Silicon with Erbium: Pores Filling as a Method to Limit the Er-clustering Effects and Increasing its Light Emission. *Sci. Rep.* **2017**, *7*, 5957–5969.
- (36) Li, Y.; Xiao, X.; Ye, Z. Facile Fabrication of Tetragonal Scheelite (t-s)  $\text{BiVO}_4/\text{g-C}_3\text{N}_4$  Composites with Enhanced Photocatalytic Performance. *Ceram. Int.* **2018**, *44*, 7067–7076.
- (37) Tokunaga, S.; Kato, H.; Kudo, A. Selective Preparation of Monoclinic and Tetragonal  $\text{BiVO}_4$  with Scheelite Structure and their Photocatalytic Properties. *Chem. Mater.* **2001**, *13*, 4624–4628.
- (38) Sun, Y.; Wu, C.; Long, R.; Cui, Y.; Zhang, S.; Xie, Y. Synthetic Loosely-packed Monoclinic  $\text{BiVO}_4$  Nanoellipsoids with Novel Multiresponses to Visible Light, Trace Gas and Temperature. *Chem. Commun.* **2009**, *30*, 4542–4544.
- (39) Beg, S.; Haneef, S.; Al-Areqi, N. Study of Electrical Conductivity and Phase Transition in  $\text{Bi}_2\text{O}_3\text{-V}_2\text{O}_5$ . *Phase Transitions* **2010**, *83*, 1114–1125.
- (40) Luo, Y.; Tan, G.; Dong, G.; Ren, H.; Xia, A. A Comprehensive Investigation of Tetragonal Gd-doped  $\text{BiVO}_4$  with Enhanced Photocatalytic Performance Under Sun-light. *Appl. Surf. Sci.* **2016**, *364*, 156–165.
- (41) Kim, T. W.; Ping, Y.; Galli, G. A.; Choi, K.-S. Simultaneous Enhancements in Photon Absorption and Charge Transport of Bismuth Vanadate Photoanodes for Solar Water Splitting. *Nat. Commun.* **2015**, *6*, 8769–8779.
- (42) Wan, X.; Niu, F.; Su, J.; Guo, L. Enhanced Photoelectrochemical Water Oxidation of Bismuth Vanadate via a Combined Strategy of W Doping and Surface RGO Modification. *Phys. Chem. Chem. Phys.* **2016**, *18*, 31803–31810.
- (43) Raiser, D.; Deville, J. P. Study of XPS Photoemission of Some Gadolinium Compounds. *J. Electron Spectrosc. Relat. Phenom.* **1991**, *57*, 91–97.
- (44) Zhao, J.; Gill, T. M.; Zheng, X. Enabling Silicon Photoanodes for Efficient Solar Water Splitting by Electroless-deposited Nickel. *Nano Res.* **2018**, *11*, 3499–3508.
- (45) Park, S. Y.; Abroshan, H.; Shi, X. J.; Jung, H. S.; Siahrostami, S.; Zheng, X.  $\text{CaSnO}_3$ : An Electrocatalyst for Two-electron Water Oxidation Reaction to Form  $\text{H}_2\text{O}_2$ . *ACS Energy Lett.* **2019**, *4*, 352–357.
- (46) Sharp, I. D.; Cooper, J. K.; Toma, F. M.; Buonsanti, R. Bismuth Vanadate as a Platform for Accelerating Discovery and Development of Complex Transition-metal Oxide Photoanodes. *ACS Energy Lett.* **2017**, *2*, 139–150.
- (47) Ding, C.; Shi, J.; Wang, D.; Wang, Z.; Wang, N.; Liu, G.; Xiong, F.; Li, C. Visible Light Driven Overall Water Splitting using Cocatalyst/ $\text{BiVO}_4$  Photoanode with Minimized Bias. *Phys. Chem. Chem. Phys.* **2013**, *15*, 4589–4595.
- (48) Lee, D. K.; Choi, K.-S. Enhancing Long-term Photostability of  $\text{BiVO}_4$  Photoanodes for Solar Water Splitting by Tuning Electrolyte Composition. *Nat. Energy* **2018**, *3*, 53–60.
- (49) Fuku, K.; Miyase, Y.; Miseki, Y.; Funaki, T.; Gunji, T.; Sayama, K. Photoelectrochemical Hydrogen Peroxide Production from Water on a  $\text{WO}_3/\text{BiVO}_4$  Photoanode and From  $\text{O}_2$  on an Au Cathode without External Bias. *Chem. - Asian J.* **2017**, *12*, 1111–1119.